JOURNAL OF THERMOPHYSICS AND HEAT TRANSFER
Vol. 20, No. 3, July–September 2006

Parametric Study of Modified Vertical Bridgman Growth in a Rotating Magnetic Field

X. Wang* and N. Ma†
North Carolina State University, Raleigh, North Carolina 27695
D. F. Bliss‡
U. S. Air Force Research Laboratory, Hanscom AFB, Massachusetts 01731
G. W. Iseler§
Iseler Associates, Chelmsford, Massachusetts 01824
and
P. Becla¶
Solid State Scientific, Hollis, New Hampshire 03049

Using the vertical Bridgman process, a single semiconductor crystal is grown by the solidification of an initially molten semiconductor (melt) contained in a crucible. In addition to the main Bridgman heater, a submerged heater is added that separates the melt into two zones, i.e., an upper melt and a lower melt that is continuously replenished with fluid from the upper melt to offset the rejection of species along the crystal–melt interface. As crystal growth progresses, the crucible is slowly lowered to maintain a constant lower melt depth. An externally applied rotating magnetic field produced by a synchronous motor stator is used to control the transport of the electrically conducting molten semiconductor. This paper treats the flow of a molten semiconductor and the dopant transport during the vertical Bridgman process with a submerged heater and with a transverse rotating magnetic field. This paper also investigates the effects of the crystal radius, the melt depth, the strength of the magnetic field, and the number of poles in the inductor on the dopant distributions in the crystal.

Nomenclature

B	=	amplitude of rotating magnetic field
B_ω	=	strength of the rotating magnetic field
b	=	dimensionless depth of the melt
C	=	dimensionless concentration of the dopant in the melt
C_s	=	dimensionless concentration in the crystal
c_p	=	specific heat of the melt
D	=	diffusion coefficient for the dopant in the molten semiconductor
f	=	frequency of the ac power source
f_θ	=	dimensionless azimuthal body force
g	=	gravitational acceleration
h	=	dimensionless length of the entire crystal
J_m	=	Bessel function of the first kind and mth order
j	=	dimensionless electric current density
k	=	thermal conductivity of the melt
k_s	=	segregation coefficient for selenium in gallium-antimonide
m	=	number of pole pairs for the rotating magnetic field
$\hat{\boldsymbol{n}}$	=	outward unit normal vector
Pe_g	=	growth Péclet number
Pe_m	=	species transport Péclet number
Pr	=	Prandtl number
p	=	dimensionless pressure
R	=	crystal radius or inner radius of the crucible
Ra	=	Rayleigh number
r	=	dimensionless radial coordinate in the melt
$\hat{\boldsymbol{r}}$	=	unit vector in the radial direction for the cylindrical coordinate system
T	=	dimensionless temperature in the melt
T_h	=	uniform, constant temperature of the heater's surface
T_m	=	magnetic Taylor number
T_s	=	solidification temperature for pure gallium-antimonide
t	=	dimensionless time
U_c	=	characteristic velocity of the melt
U_g	=	constant growth rate
$\boldsymbol{v}$	=	dimensionless velocity in the melt
v_r	=	dimensionless radial velocity in the melt
v_θ	=	dimensionless azimuthal velocity in the melt
v_z	=	dimensionless axial velocity in the melt
$\hat{\boldsymbol{x}}$	=	unit vector in the horizontal direction for the Cartesian coordinate system
z	=	dimensionless axial coordinate in the melt
$\hat{\boldsymbol{z}}$	=	unit vector in the axial direction for the cylindrical coordinate system
(ΔT)	=	characteristic temperature difference
α	=	dimensionless growth rate
β	=	thermal coefficient of volumetric expansion
Γ	=	characteristic ratio of Joule heating to conductive heat transfer
γ_h	=	dimensionless radius of the submerged heater housing
Δ	=	the difference between the crystal concentration at the centerline and at the periphery after steady state
ζ	=	dimensionless rescaled axial coordinate in the melt
θ	=	dimensionless azimuthal coordinate in the melt
$\hat{\boldsymbol{\theta}}$	=	unit vector in the azimuthal direction for the cylindrical coordinate system
κ	=	thermal diffusivity of the melt
κ_1, κ_2	=	constants in the velocity profile for the gap flow
μ	=	dynamic viscosity of the melt
ν	=	kinematic viscosity of the melt
ρ	=	density of the melt

Received 19 August 2005; revision received 8 November 2005; accepted for publication 18 November 2005.

*Graduate Research Assistant, Department of Mechanical and Aerospace Engineering, Campus Box 7910.
†Assistant Professor, Department of Mechanical and Aerospace Engineering, Campus Box 7910; nancy_ma@ncsu.edu. Senior Member AIAA.
‡Physicist, AFRL/SNHC, 80 Scott Road.
§Physicist, 26 State Street.
¶Physicist, 27-2 Wright Road.

σ = electrical conductivity of the melt
Φ = steady, axisymmetric part of the dimensionless electric potential
ϕ = dimensionless electric potential
ψ = dimensionless Stokes streamfunction in the melt
ω = circular frequency of the ac electric power source

Subscripts and Superscripts

min = minimum value
max = maximum value
$*$ = dimensional value

I. Introduction

BULK gallium antimonide (GaSb) semiconductor crystals with high optical transmission are extremely important for space-based imaging applications. An investigation of the melt growth of these crystals, as well as other III–V semiconductors, is under way at the U.S. Air Force Research Laboratory at Hanscom Air Force Base. Single crystals of compound semiconductors can be produced by solidification from the melt by the Bridgman process. An element called a dopant is added to the melt during growth to give the crystal certain electrical and/or optical properties. After the crystal is solidified, the crystal ingot is sliced into wafers, which are then prepared for manufacture of optoelectronic devices. For optimal optical or wireless communication, it is critical that the radial distribution be uniform across a single wafer and that the axial distribution be uniform so that the concentration is the same from wafer to wafer. Therefore, a major objective during the growth of any semiconductor crystal is to have a controllable uniform distribution of dopant in the crystal, which depends on the convective and diffusive transport of the dopant in the melt. Because molten semiconductors are excellent electrical conductors, externally applied fields such as magnetic and electric fields can be used to control the flow of the molten semiconductor (melt). Recently, the application of rotating magnetic fields during semiconductor crystal growth has revealed an extremely promising flow phenomenon. Rotating magnetic fields can create an electromagnetic (EM) body force that provides EM stirring of the melt. This provides a means to control transport in the melt that can cause the crystal to solidify with much better properties than obtained with other traditional crystal growth methods. Salk et al.[1] and Fiederle et al.[2] made experimental investigations that applied rotating magnetic fields during crystal growth and obtained crystals with less segregation. Dold and Benz[3] reviewed the literature on the use of rotating magnetic fields during crystal growth.

Unfortunately, crystals grown by the traditional Bridgman method solidify with severe axial segregation.[4] Ostrogorsky[5] introduced a modification of the bottom-seeded Bridgman method in which a submerged heater separates the melt into two zones, namely, a lower melt and an upper melt. As crystal growth progresses, the crystal solidifies and the crucible is slowly lowered to maintain a constant lower melt depth. The lower melt is continuously replenished with liquid from the upper melt with a composition chosen to offset the increasing dopant level in the lower melt due to rejection at the crystal-melt interface for dopants with segregation coefficients less than unity. Ma et al.[6] and Wang et al.[7] have shown that this replenishment produces crystals with more radial and axial compositional uniformity. Ostrogorsky and Müller[8] have shown that this modified bottom-seeded method produces crystals with much lower defect densities than crystals grown by other methods.

A rotating magnetic field (RMF) can be applied during Bridgman crystal growth using a submerged heater. An RMF is a periodic transverse magnetic field which rotates in the azimuthal direction about the centerline of the melt. An RMF is produced by a number of magnet poles that are placed at equally spaced azimuthal positions around the crystal-growth furnace and are connected to successive phases of a multiphase ac power source. An RMF has a constant magnetic-field pattern that rotates in the azimuthal direction with an angular velocity ω/m, where ω is the circular frequency of the ac electric power source, and m is the number of pole pairs.

Previous studies[9–13] have modelled melt motion in cylindrical or Bridgman-like configurations without solidification. In the present investigation, we treat the melt motion and the species transport of a dopant in a molten semiconductor during a vertical Bridgman process with a submerged heater and with a periodic, transverse magnetic field. We use a Chebyshev spectral collocation method and provide predictions for the melt motion, for the dopant distribution in the melt at several stages during growth, and for the dopant distribution in the crystal.

II. Melt Motion

This paper treats the unsteady, axisymmetric species transport of selenium in a gallium antimonide melt during the vertical Bridgman process with a submerged heater and with an externally applied periodic transverse magnetic field, as shown in Fig. 1. A single-crystal seed, which initiates solidification, lies along the bottom of the pyrolytic boron nitride (pBN) crucible. A graphite disc and a boron nitride disc lie below the crucible. These discs are cooled by a water-cooled hearth, which removes heat along the bottom of the crucible. The coordinates and lengths are normalized by the crucible's inner radius R, which is equal to the crystal radius, so that γ_h is the dimensionless radius of the submerged fused-silica heater housing, and b is the dimensionless depth of the lower melt. The variables r, θ, and z are the cylindrical coordinates with the z-axis along the centerline of the crystal-growth furnace with unit vectors $\hat{\boldsymbol{r}}$, $\hat{\boldsymbol{\theta}}$, and $\hat{\boldsymbol{z}}$. As the crystal solidifies along $z=\alpha t$, the crucible is lowered so that the crystal–melt interface remains at the same axial position throughout growth, where the dimensionless rate is $\alpha = U_g/U_c$. Here, U_g is the constant growth rate and $U_c = \mu/\rho R$ is the characteristic velocity of the melt for a uniform density ρ and dynamic viscosity μ. The submerged heater along $z=\alpha t + b$ is stationary where t is normalized by R/U_c. The depth of the lower melt is constant throughout the growth. The lower melt is replenished with liquid supplied from the upper melt to a small annular gap between the submerged heater and the inner surface of the crucible.

A rotating magnetic field is given by $B_\omega \hat{\boldsymbol{x}} = Br^{m-1}\{\cos[m(\theta - \omega t)]\hat{\boldsymbol{r}} - \sin[m(\theta-\omega t)]\hat{\boldsymbol{\theta}}\}$. An RMF actually produces a periodic, nonaxisymmetric body force in addition to the steady, axisymmetric, azimuthal body force, but the frequency of the nonaxisymmetric part of the body force is $2mf$, where $f=\omega/2\pi$ is the frequency of the ac electric power source. The fluid cannot respond to the nonaxisymmetric part of the electromagnetic body force because this force oscillates with $2m$ times the frequency of the leading-order RMF. Witkowski et al.[10] proved that the velocity produced by the nonaxisymmetric part of the body force is negligible compared to the velocity produced by the axisymmetric part of the body force for $m=1$ because the inertia of the melt precludes the melt from responding to such a high-frequency body force. In the present study, we neglect the nonaxisymmetric part of the body force, because the velocity produced by the nonaxisymmetric part of the body force is negligible. In a frame of reference moving with the rotating magnetic field at ω/m, the body force is independent of time and the melt motion is axisymmetric and steady.

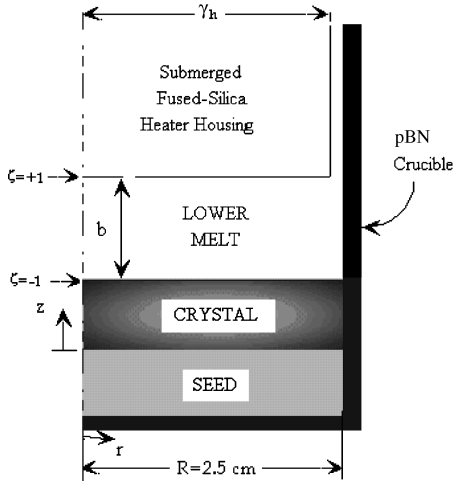

Fig. 1 Vertical Bridgman process using submerged heater growth.

The electric potential is given by $\phi(r,\theta,\zeta)=\cos[m(\theta-\omega t)]\Phi(r,\zeta)$. With the neglect of the nonaxisymmeric part, the steady, axisymmetric, azimuthal body force is

$$f_\theta=\frac{1}{2}r^{m-1}\left(r^m-\frac{\partial\Phi}{\partial z}\right) \tag{1a}$$

which is a function of $\Phi(r,\zeta)$[14]

$$\Phi(r,\zeta)=\sum_{n=1}^{\infty}\frac{2mJ_m(\lambda_n r)\sinh\left(\frac{1}{2}\lambda_n b\zeta\right)}{\lambda_n\left(\lambda_n^2-m^2\right)J_m(\lambda_n)\cosh\left(\frac{1}{2}\lambda_n b\right)} \tag{1b}$$

where Φ is normalized by $\omega BR^2/m$ and f_θ is normalized by $\sigma B^2\omega R/m$. Here, $\zeta=-1+2(z-\alpha t)/b$ is a rescaled axial coordinate so that $-1\le\zeta\le+1$. The eigenvalues λ_n are the roots of $\lambda_n J_{m-1}(\lambda_n)-mJ_m(\lambda_n)=0$. Here, J_m is the Bessel function of the first kind and mth order.

In a reference frame moving with the crystal–melt interface, with the Boussinesq approximation, the equations governing the melt motion are steady,

$$(\boldsymbol{v}\cdot\boldsymbol{\nabla})\boldsymbol{v}=-\boldsymbol{\nabla}p+T_m f_\theta\hat{\boldsymbol{\theta}}+(Ra/Pr)T\hat{\boldsymbol{z}}+\boldsymbol{\nabla}^2\boldsymbol{v} \tag{2a}$$

$$\boldsymbol{\nabla}\cdot\boldsymbol{v}=0 \tag{2b}$$

$$\boldsymbol{v}\cdot\boldsymbol{\nabla}T=(1/Pr)\boldsymbol{\nabla}^2T+\Gamma j^2 \tag{2c}$$

for $0\le r\le1$ and $\alpha t\le z\le\alpha t+b$, where the melt velocity $\boldsymbol{v}=v_r\hat{\boldsymbol{r}}+v_\theta\hat{\boldsymbol{\theta}}+v_z\hat{\boldsymbol{z}}$ is normalized by U_c, p is the deviation of the pressure from the hydrostatic pressure normalized by $\mu^2/\rho R^2$, and T is the deviation of the temperature from the solidification temperature T_s normalized by characteristic temperature difference $(\Delta T)=(T_h-T_s)$ with the uniform, constant temperature T_h for the melt adjacent to the heater. The dimensionless parameters in Eqs. (2a) and (2c) are the magnetic Taylor number $T_m=\sigma\omega B^2R^4/m\rho\nu^2$, the Rayleigh number $Ra=g\beta(\Delta T)R^3/\nu\kappa$, and the Prandtl number $Pr=\nu/\kappa$. Here, $g=9.81\ \mathrm{m/s^2}$, whereas the kinematic viscosity and thermal diffusivity of the melt are $\nu=\mu/\rho$ and $\kappa=k/\rho c_p$, respectively, where k, c_p, β, and σ are the thermal conductivity, the specific heat, the thermal volumetric expansion coefficient, and the electrical conductivity of the melt, respectively. In Eq. (2c), j is the electric current density normalized by $\sigma B\omega R/m$ and the characteristic ratio of Joule heating to conductive heat transfer is $\Gamma=\sigma B^2\omega^2R^4/m^2k(\Delta T)$. For the present process with $\omega=120\pi$ rad/s, $R=2.5$ cm, $(\Delta T)=20$ K, $B=2$ mT, and $m=1$, $\Gamma=0.001623$, so that Joule heating is negligible.

The no-slip and no-penetration conditions along the crucible are

$$v_r=v_\theta=0,\qquad \text{at}\ r=1,\qquad \text{for}-1\le\zeta\le+1 \tag{3a, 3b}$$

$$v_z=-\alpha,\qquad \text{at}\ r=1,\qquad \text{for}-1\le\zeta\le+1 \tag{3c}$$

The boundary conditions on the crystal–melt interface and on the surface of the fused-silica heater are

$$v_r=v_\theta=0,\qquad \text{at}\ \zeta=-1,\qquad \text{for}\ 0\le r\le1 \tag{4a, 4b}$$

$$v_z=-\alpha,\qquad \text{at}\ \zeta=-1,\qquad \text{for}\ 0\le r\le1 \tag{4c}$$

$$v_r=v_\theta=0,\qquad \text{at}\ \zeta=+1,\qquad \text{for}\ 0\le r\le1 \tag{4d, 4e}$$

$$v_z=0,\qquad \text{at}\ \zeta=+1,\qquad \text{for}\ 0\le r\le\gamma_h \tag{4f}$$

Assuming that the density of the crystal and melt are the same, the gap between the heater and the crucible replenishes the solidifying melt at a volumetric flowrate $\pi\alpha$, so that we assume a simple velocity profile,[6]

$$v_z=\alpha[-1+\kappa_1(1-r)+\kappa_2(1-r^2)]\qquad \text{at}\ \zeta=+1,\qquad \text{for}\ \gamma_h\le r\le1 \tag{5}$$

where $\kappa_1=3(1+\gamma_h^2)/(1-\gamma_h)^3$ and $\kappa_2=-2(1+\gamma_h+\gamma_h^2)/(1-\gamma_h)^3(1+\gamma_h)$.

The submerged heater above the lower melt and the heaters adjacent to the periphery of the crucible are adjusted so that the crystal–melt interface is planar, and the melt adjacent to the submerged heater is held at a uniform and constant temperature T_h. Therefore, thermal boundary conditions are

$$T=0,\qquad \text{at}\ \zeta=-1,\qquad \text{for}\ 0\le r\le1 \tag{6a}$$

$$T=1,\qquad \text{at}\ \zeta=+1,\qquad \text{for}\ 0\le r\le1 \tag{6b}$$

$$\frac{\partial T}{\partial r}=0,\qquad \text{at}\ r=1,\qquad \text{for}-1\le\zeta\le+1 \tag{6c}$$

The heaters are adjusted so that the rate of heat transfer from the crucible to the melt is negligible.

We introduce a Stokes stream function for the radial and axial velocities,

$$v_r=\frac{1}{r}\frac{\partial\psi}{\partial z},\qquad v_z=-\frac{1}{r}\frac{\partial\psi}{\partial r} \tag{7a, 7b}$$

which identically satisfies conservation of mass for our axisymmetric melt motion. For a given value of T_m, we solved for v_θ, ψ, and T using a Chebyshev spectral collocation method[15,16] with Gauss–Lobatto collocation points in r and ζ. Since Eqs. (2a) and (2c) are nonlinear, we used a Newton–Raphson iterative method and incrementally increased T_m from zero. After the Newton–Raphson method converged for a given T_m, we used a continuation method to obtain initial guesses for the coefficients in the spectral representations for $(T_m+\Delta T_m)$. For each value of T_m, the numbers of collocation points were varied in order to ensure that the results were independent of this number and to insure that all boundary layers were adequately resolved.

III. Dopant Transport

Before solidification begins, the dopant concentration is uniform, and this initial value is used to normalize the concentration C, so that $C(r,z,t=0)=1$. The equation governing the dopant transport is

$$\frac{\partial C}{\partial t}+\boldsymbol{v}\cdot\nabla C=Pe_m^{-1}\nabla^2C \tag{8}$$

where $Pe_m=U_cR/D$ is the mass Péclet number. Here, D is the diffusion coefficient for the dopant in the molten semiconductor. The boundary condition for the crystal–melt interface is

$$\frac{2}{b}\frac{\partial C}{\partial\zeta}=Pe_g(k_s-1)C,\qquad \text{at}\ \zeta=-1,\qquad \text{for}\ 0\le r\le1 \tag{9}$$

where $Pe_g=U_gR/D=\alpha Pe_m$ is the growth Péclet number and k_s is the segregation coefficient for the dopant in the molten semiconductor. Once crystal growth begins, the selenium is rejected into the melt and the concentration of the dopant in the melt rises. In order to compensate for this elevated level of dopant, the melt is replenished with dopant-depleted melt, so that the boundary condition at the gap between the heater and the crucible is

$$C=k_s,\qquad \text{at}\ \zeta=1,\qquad \text{for}\ \gamma_h\le r\le1 \tag{10}$$

where $k_s=0.1$ for gallium antimonide doped with selenium. The boundary conditions along the surfaces of the crucible and fused-silica heater are $\hat{\boldsymbol{n}}\cdot\boldsymbol{\nabla}C=0$, where $\hat{\boldsymbol{n}}$ is the outward unit normal vector. We use a Chebyshev spectral collocation method with a second-order implicit time integration scheme to solve Eq. (8) with

Gauss–Lobatto collocation points in r and ζ. We use a sufficient number of collocation points to resolve the concentration gradients near the boundaries. We integrate from $t=0$ to a t that is slightly less than h/α, where h is the dimensionless length of the crystal. We use a large enough number of time steps so that the results do not change by increasing the number of time steps.

Assuming that the dopant does not diffuse in the solid crystal and that the density of the solid and liquid are the same, the concentration in the crystal $C_s(r,z)$, normalized by the initial uniform dopant concentration in the melt, is $C_s(r,z)=k_sC(r,\zeta=-1,t=z/\alpha)$. The first-grown part of the crystal solidifies at $t=0$ with $C_s(r,0)=k_s$.

IV. Results

We present results for a typical process for which the crystal length is 8 cm, the growth rate is 2 mm/h, and the frequency of the ac power source is 60 Hz, and with the thermophysical properties of molten gallium antimonide, for which $Pr=0.0443$. We investigate the effects of the crystal radius, melt depth, magnetic field strength, and number of poles on the transport. The parameters are $b=0.01R^{-1}$, $\gamma_h=0.02R^{-1}$, $h=0.08R^{-1}$, $U_c=3.8308\times10^{-7}R^{-1}$, $Ra=5.6731\times10^{9}R^{3}$, $T_m=4.2602\times10^{17}B^2R^4m^{-1}$, $Pe_g=27.778R$, $\alpha=1.4502R$, and $h/\alpha=0.05516R^{-2}$, with R in m and B in T.

We present the results for $R=2.5$ cm, $\gamma_hR=2$ cm, $bR=1$ cm, $B=2$ mT, and $m=1$ for which $b=0.4$, $\gamma_h=0.8$, $h=3.2$, $U_c=0.00001532$ m/s, $Ra=88{,}641.4$, $T_m=665{,}647.8$, $Pr=0.0443$, $Pe_m=19.1542$, $Pe_g=0.6944$, $\alpha=0.036255$, and the dimensionless time to grow the crystal is $h/\alpha=88.2627$.

In Fig. 2, we present the contours for the steady melt motion. In Fig. 2a, the isotherms reflect a purely axial temperature gradient, so that there is no thermal buoyant convection. The azimuthal electromagnetic body force f_θ drives an azimuthal velocity that is presented in Fig. 2b, where the maximum value of v_θ is 163.62. The meridional melt motion is driven by the gap flow and by the RMF. The inertial effects augment viscous opposition to the constant driving force due to the gap flow. The meridional melt motion is split into two opposing circulations as shown in Fig. 2c, where the upper circulation flows in the counterclockwise direction and the lower circulation flows in the clockwise direction. In Fig. 2c, the minimum and maximum values of the meridional streamfunction are $\psi_{\min}=-0.6783$ and $\psi_{\max}=0.7015$, respectively.

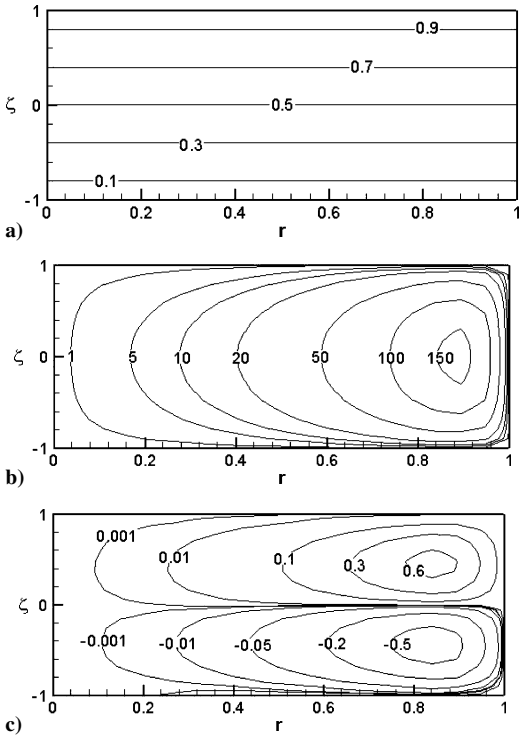

Fig. 2 Contours for the steady melt motion with $R=2.5$ cm, $\gamma_hR=2$ cm, $bR=1$ cm, $B=2$ mT, and $m=1$: a) temperature $T(r,\zeta)$, b) azimuthal velocity $v_\theta(r,\zeta)$, and c) meridional streamfunction $\psi(r,\zeta)$.

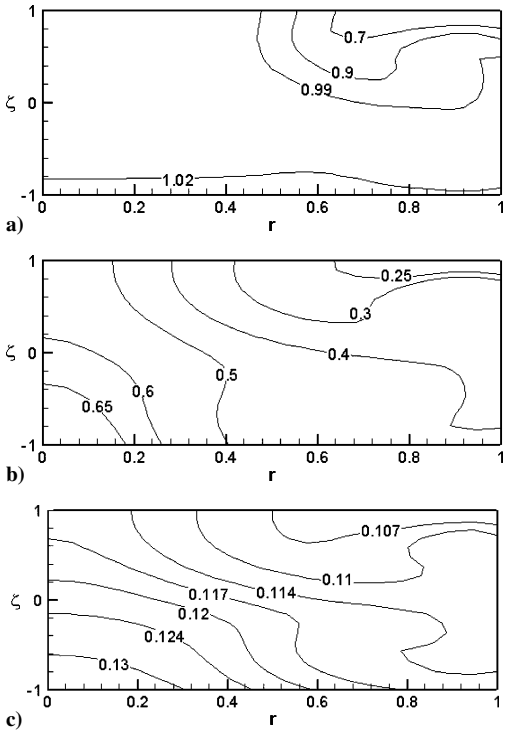

Fig. 3 Constant-concentration curves in the melt with $R=2.5$ cm, $\gamma_hR=2$ cm, $bR=1$ cm, $B=2$ mT, and $m=1$: a) concentration $C(r,\zeta,t=0.05516)$, b) concentration $C(r,\zeta,t=1.7653)$, c) concentration $C(r,\zeta,t=15.722)$.

The constant-concentration curves in the melt at $t=0.05516$ when 0.0625% of the crystal has grown are presented in Fig. 3a. The minimum value of the concentration is always equal to $k_s=0.1$ because the melt is replenished with fluid having concentration $C=k_s$ at $\zeta=+1$ for $\gamma_h\le r\le1$. The melt adjacent to the gap is dopant-depleted with $C<1$. The melt adjacent to the crystal–melt interface at $\zeta=-1$ is dopant-rich with $C>1$ because the interface has rejected the dopant upon solidification. The maximum value of the concentration in the melt at this time is $C_{\max}=1.04203$. The majority of the melt still has initial uniform concentration $C=1$ because the dopant has not had time to convect or diffuse into the bulk of the melt.

In Fig. 3b, we present the constant-concentration curves in the melt at $t=1.7653$ when 2% of the crystal has grown. At this time, the dopant-depleted melt has convected or diffused over the entire volume of the melt and the maximum value of the concentration is $C_{\max}=0.7064$. By the time 17.8% of the crystal has grown at $t=15.722$, the dopant transport has reached a steady state. The constant-concentration curves in the melt at this time are presented in Fig. 3c and these contours remain the same for the remainder of growth.

In Fig. 4, we present the constant-concentration curves in the crystal. There is small radial segregation in the first-grown section of the crystal before the melt motion reaches the steady state. The concentration is always higher at the centerline compared with the periphery of the crystal, and this difference is $\Delta=C_s(0,3.1998)-C_s(1,3.1998)=0.001934$ for the last-grown section of the crystal which solidified after steady-state transport had been reached in the melt. Steady-state dopant transport has been achieved when 17.8% of the crystal has grown, so that the top 82.2% of the crystal is axially uniform and solidifies with the same radial dopant distribution.

We investigate the effects of different parameters on the melt motion and dopant transport. Table 1 presents the maximum value of the dimensional EM body force $f_{\theta,\max^*}$, the maximum magnitude of the dimensional velocity $v_{\max^*}$, and the crystal's radial segregation after the dopant transport has reached a steady state Δ. As the magnetic field strength increases, the EM body force increases the stirring in the melt so that the crystal's radial segregation after steady

Table 1 Maximum value of the EM body force and the magnitude of the velocity and the crystal's radial segregation versus various parameters

Case	bR, cm	$\gamma_h R$, cm	R, cm	B, mT	$2m$	$f_{\theta,\max^*}$, N/m^3	$v_{\max^*}$, cm/s	Δ
a	1	2	2.5	0	2	0	0.000742	0.003485
b	1	2	2.5	1.0	2	0.74414	0.06696	0.003373
c	1	2	2.5	2.0	2	2.97656	0.25131	0.001934
d	1	1.5	2.5	2.0	2	2.97656	0.25127	0.001827
e	1	1.75	2.5	2.0	2	2.97656	0.25128	0.001866
f	1	2.25	2.5	2.0	2	2.97656	0.25134	0.002152
g	2	2	2.5	2.0	2	6.1994	0.8832	0.0004772
h	3	2	2.5	2.0	2	9.3127	1.6159	0.0002635
i	1	2	2.5	2.0	4	2.8860	0.2122	0.002257
j	1	2	2.5	2.0	6	2.7521	0.1752	0.002572
k	1	2	3	2.0	6	2.7938	0.1866	0.003846

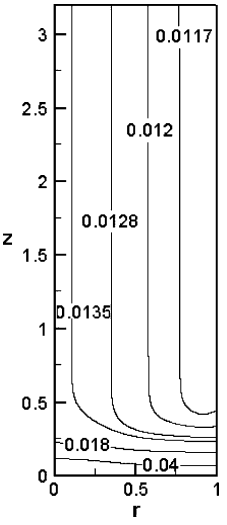

Fig. 4 Constant-concentration curves in the crystal for $R = 2.5$ cm, $\gamma_h R = 2$ cm, $bR = 1$ cm, $B = 2$ mT, and $m = 1$.

state decreases, as reflected in cases a, b, and c. When the radius of the submerged heater increases, the melt motion is almost the same because the meridional melt motion due to the EM stirring is significantly stronger than the gap flow. However, a smaller volume of dopant is replenished through the gap so that the crystal's radial segregation increases as the radius of the submerged heater increases, as reflected in cases b, d, e, and f. As the melt depth increases, the EM body force increases and the crystal's radial segregation decreases. When we double or triple the melt depth, the radial segregation decreases by an order in magnitude, as reflected in cases b, g, and h. As the number of poles increases, the EM body force and stirring decreases and crystal's radial segregation increases, as reflected in cases b, i, and j. Another important parameter that affects the melt motion is the radius of the crystal. When the radius of the crystal increases by 20% from 2.5 to 3 cm, the crystal's radial segregation increases, as reflected in cases j and k.

V. Conclusions

We have developed a numerical model that can predict steady transport in the melt, unsteady dopant transport in the melt, and dopant distribution in the crystal during the vertical Bridgman process with a submerged heater and with a transverse, rotating magnetic field. Future research will compare model predictions with experimental data for the dopant concentration in the crystal. After the melt motion reaches steady state, the remainder of the crystal solidifies with the same radial dopant distribution. The radial segregation in the crystal decreases as the strength of the rotating magnetic field increases, as the width of the gap increases, as the number of magnet poles decreases, as the radius of the crystal decreases, and as the depth of the melt increases.

Acknowledgments

This research was supported by the U. S. Air Force Office of Scientific Research under Grant FA9550-04-1-0249. The calculations were performed on the Cray X1 provided by the DoD High Performance Computing Modernization Program under Grant AFSNH2487 and on the IBM pSeries 690 provided by the National Computational Science Alliance under Grant DMR030015.

References

[1]Salk, M., Fiederle, M., Benz, K. W., Senchenkov, A. S., Egorov, A. V., and Matioukhin, D. G., "CdTe and $CdTe_{0.9}Se_{0.1}$ Crystals Grown by the Travelling Heater Method Using a Rotating Magnetic Field," *Journal of Crystal Growth*, Vol. 138, No. 1/4, 1994, pp. 161–167.

[2]Fiederle, M., Eiche, C., Joerger, W., Salk, M. Senchenkov, A. S., Egorov, A. V., Ebling, D. G., and Benz, K. W., "Radiation Detector Properties of $CdTe_{0.9}Se_{0.1}$: Cl Crystals Grown Under Microgravity in a Rotating Magnetic Field," *Journal of Crystal Growth*, Vol. 166, No. 1/4, 1996, pp. 256–260.

[3]Dold, P., and Benz, K. W., "Rotating Magnetic Fields: Fluid Flow and Crystal Growth Applications," *The Role of Magnetic Fields in Crystal Growth, Progress in Crystal Growth and Characterization*, Vol. 38, No. 1/4, edited by K. W. Benz, Oxford, Elsevier, 1999, pp. 7–38.

[4]Wang, X., and Ma, N., "Strong Magnetic Field Asymptotic Model for Binary Alloyed Semiconductor Crystal Growth," *Journal of Thermophysics and Heat Transfer*, Vol. 18, No. 4, 2004, pp. 476–480.

[5]Ostrogorsky, A. G., "Numerical Simulation of Single Crystal Growth by Submerged Heater Method," *Journal of Crystal Growth*, Vol. 104, No. 2, 1990, pp. 233–238.

[6]Ma, N., Bliss, D. F., and Iseler, G. W., "Vertical Gradient Freezing of Doped Gallium-Antimonide Semiconductor Crystals Using Submerged Heater Growth and Electromagnetic Stirring," *Journal of Crystal Growth*, Vol. 259, No. 1/2, 2003, pp. 26–35.

[7]Wang, X., Ma, N., Bliss, D. F., and Iseler, G. W., "Semiconductor Crystal Growth by Modified Vertical Gradient Freezing with Electromagnetic Stirring," *Journal of Thermophysics and Heat Transfer*, Vol. 19, No. 1, 2005, pp. 95–100.

[8]Ostrogorsky, A. G., and Müller, G., "Normal and Zone Solidification Using the Submerged Heater Method," *Journal of Crystal Growth*, Vol. 137, No. 1/4, 1994, pp. 64–71.

[9]Mossner, R., and Gerbeth, G., "Buoyant Melt Flows under the Influence of Steady and Rotating Magnetic Fields," *Journal of Crystal Growth*, Vol. 197, No. 1/2, 1999, pp. 341–354.

[10]Witkowski, L. M., Walker, J. S., and Marty, P., "Nonaxisymmetric Flow in a Finite-Length Cylinder with a Rotating Magnetic Field," *Physics of Fluids*, Vol. 11, No. 7, 1999, pp. 1821–1826.

[11]Walker, J. S., Volz, M. P., and Mazuruk, K., "Raleigh–Benard Instability in a Vertical Cylinder with a Rotating Magnetic Field," *International Journal of Heat and Mass Transfer*, Vol. 47, No. 8/9, 2004, pp. 1877–1887.

[12]Ma, N., Walker, J. S., Lüdge, A., and Riemann, H., "Combining a Rotating Magnetic Field and Crystal Rotation in the Floating–Zone Process with a Needle-Eye Induction Coil," *Journal of Crystal Growth*, Vol. 230, No. 1/2, 2001, pp. 118–124.

[13]Ghaddar, C. K., Lee, C. K., Motakef, S., and Gillies, D. C., "Numerical Simulation of THM Growth of CdTe in Presence of Rotating Magnetic Fields (RMF)," *Journal of Crystal Growth*, Vol. 205, No. 1/2, 1999, pp. 97–111.

[14]Marty, P. H., Witkowski, L. M., Trombetta, P., Tomasino, T., and Garandet, J. P., *Transfer Phenomena in Magnetohydrodynamic and Electroconducting Flows*, Kluwer Academic, Boston, 1999, pp. 327–343.

[15]Boyd, J. P., "Chebyshev and Fourier Spectral Methods," *Lecture Notes in Engineering*, edited by Brebbia, C. A., and Orszag, S. A., Springer-Verlag, New York, 1989.

[16]Canuto, C., Hussaini, M. Y., Quarteroni, A., and Zang, T. A., *Spectral Methods in Fluid Dynamics*, Springer-Verlag, New York, 1988.